Supplementary Information for

Metastable-solid phase diagrams derived from polymorphic solidification kinetics

Babak Sadigh, Luis Zepeda-Ruiz, Jonathan L. Belof

To whom correspondence should be addressed: Babak Sadigh, Jonathan L. Belof.
E-mail: sadigh1@llnl.gov, belof1@llnl.gov

This PDF file includes:

Supplementary text
Figs. S1 to S15
References for SI reference citations

Supporting Information Text

Thermodynamic phase diagram

The temperature-pressure phase diagram of the EAM model system has been directly calculated from two-phase (solid-liquid) coexistence simulations. For this purpose, we have performed simulations in an isobaric-isoenthalpic (NPH) ensemble ([1–4]). This can be considered a closed ensemble, as there is no energy exchange with an external bath, since the total system's enthalpy is kept fix. At the bulk melting point T_m, the free energies of the liquid and the solid phases are equal. However, the enthalpy of the solid H_S^m is lower than that of the liquid H_L^m. This discrepancy is observed in real-world experiments as latent heat $\Delta H_m = H_L^m - H_S^m$, released during the crystallization process. If the total enthalpy of the simulation cell H_{sys} is chosen in the range $H_S^m < H_{sys} < H_L^m$, the system will necessarily equilibrate into a solid-liquid coexistence. For an S-L coexistence with flat boundaries, it can readily be shown that the system temperature equilibrates at T_m ([5]). Such an S-L equilibrium can be established by designing an elongated computational cell, with H_{sys} chosen in the neighborhood of $1/2\left(H_S^m + H_L^m\right)$.

For the calculation of the fcc-liquid coexistence line, we have chosen computational cells containing 160,000 atoms, composed of $20 \times 20 \times 100$ primitive fcc unit cells with 4 atoms in each cell, which are arranged through stacking of fcc (001) layers. For the bcc-liquid line, computational cells containing 216,000 atoms have been used that are composed of $30 \times 30 \times 120$ primitive bcc unit cells with 2 atoms per cell, arranged through stacking of bcc (001) layers. The hcp-liquid coexistence line has been obtained via computational cells containing 83200 atoms, composed of $26 \times 50 \times 16$ hcp orthorhombic unit cells with 4 atoms per cell that are arranged by stacking hcp-$(11\bar{2}0)$ layers. The orthorhombic hcp unit cell has the lattice vectors: $\mathbf{a_1} = (0, 0, c/a)$, $\mathbf{a_2} = (1, 0, 0)$, $\mathbf{a_3} = (0, \sqrt{3}, 0)$. In the ideal hcp crystal $c/a = \sqrt{8/3}$.

Recall now that the free energies of non-pathological single-phase systems decrease monotonically with temperature, and the liquid free energy due to its larger entropy slopes down steeper than the free energy of any solid phase. Hence the free energy curves of the liquid and every solid phase ϕ cross at one and only one point T_m^ϕ. Consequently, the thermodynamic melting point T_m coincides with the highest T_m^ϕ.

It is thus found that the phase with the highest T_m is the fcc phase at $P < 71.6$ GPa, the hcp phase in the interval $71.6 < P < 85$ GPa, and the bcc at $P > 85$ GPa. Figure S1 shows the melt lines of the three phases bcc, fcc and hcp in the pressure range 40-100 GPa. We observe three triple points, one at 71.6 GPa and 3320 K, where liquid-hcp-fcc coexist, and one at 85 GPa and 3598 K, where liquid-hcp-bcc are at three-phase equilibrium. There also exists an fcc-bcc-liquid triple point at 79.5 GPa and 3478 K. It is slightly lower than the hcp melting point of 3487 K at this pressure, and therefore does not appear in the thermodynamic phase diagram, see Fig. 1 in the main text. Of course, these numbers are so close to each other that in practice, all four phases in the vicinity of 80 GPa can be considered thermodynamically stable.

A consequence of locating a triple point along the melt line is that it can be used as the starting point for integration of the phase boundary $T_{cx}(P)$ of the two coexisting crystal phases P_1 and P_1, using the Clausius-Clapeyron relation, according to which, the slope of the phase boundary is related to the ratio of the latent volume to the latent heat of the transition between the two phase:

$$\frac{dT_{cx}}{dP} = T_{cx} \left. \frac{\omega_{P_1} - \omega_{P_2}}{H_{P_1} - H_{P_2}} \right|_{T_{cx}, P} \tag{1}$$

Above, ω_{P_1} and H_{P_1} denote the volume and the enthalpy per atom at pressure P and the coexistence temperature $T_{cx}(P)$ for phase P_1.

We have calculated the hcp-bcc and the fcc-bcc phase boundaries by integration of Eq. 1 with 5 GPa and 10 GPa pressure increments respectively, Each equilibrium volume/enthalpy calculation involved averaging over a 1 ns MD-NPT simulation for the hcp-bcc and 2 ns for the fcc-bcc boundary, corresponding to 1000000 and 2000000 time steps respectively. The simulation supercells consisted of $20 \times 20 \times 20$ bcc unit cells (16000 atoms), $20 \times 20 \times 20$ fcc unit cells (32000 atoms), and $22 \times 13 \times 14$ orthorhombinc hcp unit cells (16016 atoms). Each integration started from the triple point of that boundary. They are shown in Fig. S1, as well as in Fig. 1 of the main text. The coexistence lines have substantial curvatures. The hcp-bcc line starting at 85 GPa, has a slope of nearly 11 K/GPa, which shrinks monotonically to about 6 K/GPa at 170 GPa. The fcc-bcc line has a smaller slope of 5.3 K/GPa at 80 GPa, which further decreases to 0.9 K/GPa at 120 GPa, and then rises again and exceeds 3 K/GPa at 160 GPa. The hardest phase boundary to calculate accurately is the fcc-hcp line, which is nearly vertical, due to the similarity of the two phases, and its calculation requires small preessure increments. Figure S2 shows the fcc-hcp energy differences per atom at 0 K, which exhibits a transition pressure of 50 GPa. In the same pressure range at 0 K, the bcc phase is much higher in energy: 0.0455 eV/atom above fcc at 0 GPa. This energy difference decreases only slightly with pressure. At 100 GPa, it becomes 0.0395 eV/atom.

Let us digress briefly here to discuss in some detail the algorithm we devised for efficient computation of the hcp-fcc coexistence line. As mentioned earlier, the two-phase simulations revealed an fcc-hcp-liquid triple point at 71.6 GPa and 3320 K. Performing equilibrium solid-phase simulations using the same fcc and hcp simulation cells as described above at this condition with simulation times of 2 ns, and using Eq. 1, we calculate the pressure-derivative of the hcp-fcc coexistence-line at the triple point $\dot{T}_{cx}(71.6) = 101.36$ K/GPa. Combining this with the fcc-hcp energy difference at 0 K, which becomes zero at 50 GPa, see Fig. S2, we can make a first ansatz for the shape of the line:

$$T_{cx}^{(0)}(P) = 3320 + 101.36\,(P - 71.6) - 2.42332\,(P - 71.6)^2. \tag{2}$$

Next we improve the fidelity of this approximation by choosing an intermediate pressure, e.g. 60 GPa, where we calculate at several temperatures, e.g. 1876 K, 1990 K, 2036 K, 2448, the equilibrium volumes and enthalpies of the two phases and

plug into Eq. 1 to obtain four candidate phase-coexistence slopes at $P = 60$ GPa, which we denote in the following by $\dot{T}_{60}(T)$. Through a line fit to this data, we obtain the following equation for the dependence of the slope of the coexistence line at 60 GPa on the coexistence temperature

$$\dot{T}_{60}(T) = -64.6834 + 0.0969619T. \tag{3}$$

Note that $T_{\text{cx}}^{(0)}(60) \approx 1818$. We now make an improved ansatz

$$T_{\text{cx}}^{(1)}(P) = 3320 + 101.36 \ (P - 71.6) + C \ (P - 71.6)^2 + D \ (P - 71.6)^3. \tag{4}$$

The two unknown coefficients C and D can now be determined by the two known relations: Eq. 3 and $T_{\text{cx}}(50) = 0$. The result is $C = 1.9338$ and $D = 0.2017$. Consequently, $T^{(1)}(60) = 2090$. We chose to stop at this level. But this procedure can be continued for systematic improvement of the phase line.

We have also independently verified the fcc-bcc phase boundary calculated above at three pressures, 80, 120, and 180 GPa with thermodynamic integration from bcc to fcc along the Bain path. Good agreement between the two methods has been found.

For a more in-depth view of the multiphase thermodynamics of the EAM model-Cu system, we redraw its thermodynamic phase diagram in the temperature-density plane, see Fig. S3. Furthermore, the pressure dependences of the latent volumes and latent heats of melting are shown in Figs. S4 and S5. Note the discontinuous jumps at the triple points. In particular, the specific volume of the hcp phase is smaller than the fcc phase by about 0.14% at their triple point. At 0 K this discrepancy increases to nearly 0.3% at 70 GPa.

SCL basins and thermodynamics of multiphase metastable equilibria

It is interesting to note that pure bcc and fcc metastable clusters embedded in liquid are homogeneous single-phase solids both in their cores and at their interfaces with the melt. This is in contrast to previous studies of solidification in the Lennard-Jones system (6–8), where critical nucleation on the order of thousand atoms was induced by order-parameter-based (Q_6) umbrella sampling, and it was found that the fcc critical nuclei interface the liquid through a bcc shell. We have studied fcc and bcc nuclei coexisting with liquid at pressures ranging from 0 (20 for bcc) to 100 GPa, and sizes ranging from a few thousand to nearly a million. They are all nearly spherical in shape and exhibit negligible structural heterogeneity at the liquid-solid interfaces. However, when examining the hcp clusters, see Fig. 3(c) in the main text, we find that the hcp-(0001) facets interface the liquid by transforming to fcc-(111). The appearance of an fcc shell structure at the hcp/liquid interface for only certain orientations is a clear manifestation of strong hcp/liquid interfacial anisotropy.

In order to rationalize the fcc shell structure on the hcp-(0001) facets, we have calculated the stacking fault energies in the hcp phase at 0 K as shown in Fig. S6. It displays the energetics of an intrinsic and an extrinsic stacking fault in the hcp crystal. In order to understand the atomic arrangements in these structure, one needs to know that there is degeneracy in optimal stacking of close-packed planes of hard spheres. The hcp phase corresponds to the periodic AB stacking, and the fcc phase to the periodic ABC stacking. An intrinsic stacking fault in the hcp phase can be formed by the non-periodic ..ABABCBCB.. stacking of the (0001) planes, while an extrinsic stacking fault corresponds to inserting a C plane into the structure to obtain ..ABABCABAB.. The stacking fault energies shown in Fig. S6 are an order of magnitude smaller than the fcc-liquid interfacial free energies, which range from 382 ergs/cm^2 at 40 GPa to 525 ergs/cm^2 at 80 GPa, using the Turnbull coefficient of 0.54 as calculated in the main text. As was noted in the previous section, the volume mismatch between the hcp and the fcc stacking only descreases with temperature, and there is no reason to believe temperature will markedly incease the stacking fault free energies. We have nevertheless studied the stability of a periodic 7-layer extrinsic stacking fault approximant ABABCAB, at 80 GPa by calculating its melting point via two-phase simulations and comparing it with those of the hcp and the fcc phases. The periodic slab supercells used for these simulations contained 91000 atoms with similarly elongated shapes as previously described for hcp-liquid two-phase simulations. The calculated melting point for this structure was 3487 K, to be compared with the fcc melting point of 3489 K and the hcp melting point of 3497 K. This implies that the free energy cost of growing fcc shells in the interface region between an hcp substrate and the liquid is quite small. As a result, it is reasonable to expect that there exist MSCL basins that contain clusters composed of mixed fcc/hcp stackings in equilibrium with the liquid. An example of such a cluster is shown in Fig. 3(d) in the main text. It is important to note that these basins are distinct and weakly coupled to each other and to the single-phase MSCLs illustrated in Figs. 4(a)-(c) in the main text.

The main question that now arises is whether there are mixed bcc/closed-packed MSCL basins. While it is quite easy to imagine mixed bcc/close-packed configurations, such as shown in Fig. S7, we have not been able to find a solid-liquid metastable (long-lived) equilibrium with the solid phase comprised of close-packed and bcc regions in coexistence. The configuration shown in Fig. S7 was generated in a simulation box containing 314928 particles at 60 GPa that initially contained a pure bcc cluster at equilibrium with liquid in the NPH ensemble. The cluster was slowly shrunk by reducing the total enthalpy of the NPH ensemble until no discernible solid cluster was left in the simulation box. Then the ensemble was switched to NPT, and the temperature was dropped down to 2200 K, corresponding to the homogeneous nucleation start temperature T_{HS} at 60 GPa. Subsequently, nucleation and growth of a mixed bcc/fcc cluster occurred, which is shown in Fig. S7. Once the cluster size exceeded 30000 particles, the ensemble was switched back to NPH and the multiphase system was equilibrated for over 1 ns at 60 and 80 GPa. At 60 GPa, the bcc fraction of the cluster gradually vanished during relaxation. In contrast, equilibration of the mixed bcc/fcc/hcp cluster at 80 GPa, lead to gradual disappearance of the fcc and hcp parts, and eventually a pure bcc-liquid two-phase equilibrium was obtained. We thus conclude that while the mixed-phase bcc/close-packed clusters can be

generated by kinetic processes for short times, they are not metastable, and rather belong to the transient region between two MSCL basins.

Solid-nucleation phase boundaries

In order to better understand the structure of the solutions of Eq. 12 of the main text, we elaborate below on explicit expressions for its left-hand side. The right-hand side (RHS) is small and can be treated as a perturbation. We start by expressing the excess free energy $\Delta G_{\mathrm{S}}(N_{\mathrm{S}})$ of a solid-liquid equilibrium composed of a solid nucleus of size N_{S} embedded in the melt, by a first-order expansion in deviation of the undercooling temperature T from the melting point T_m (see Eq. 7 in the main text), and using the Turnbull ansatz for the interfacial free energy Eq. 9 of the main text:

$$\Delta G_{\mathrm{S}}(T) = N_{\mathrm{S}} \frac{\Delta H_m}{T_m}(T - T_m) + \left(36\pi N_{\mathrm{S}}^2\right)^{2/3} \frac{\Delta H_m}{v_{\mathrm{S}}^{2/3}} \alpha. \tag{5}$$

By combining the generalized Gibbs-Thomson relation Eq. 6 of the main text, with the Turnbull ansatz Eq. 9 of the main text, we obtain

$$N_{\mathrm{S}}(T) = \frac{32\pi}{3} \left(\frac{T_m \, \alpha}{T_m - T}\right)^3. \tag{6}$$

Inserting the above into Eq. 5, we find the following zeroth-order solution $T_{\mathrm{cp}}^{*(0)}$ of Eq. 12 in the main text, i.e. when its RHS is set to zero

$$\frac{T_{\mathrm{cp}}^{*(0)} - T_m^{\mathrm{cp}}}{T_{\mathrm{cp}}^{*(0)} - T_m^{\mathrm{bcc}}} = \frac{T_m^{\mathrm{cp}}}{T_m^{\mathrm{bcc}}} \sqrt{\left(\frac{\alpha_{\mathrm{cp}}}{\alpha_{\mathrm{bcc}}}\right)^3 \frac{\Delta H_m^{\mathrm{cp}}}{\Delta H_m^{\mathrm{bcc}}}}. \tag{7}$$

The above represents the equation of the thermodynamic solid-solid (cp-bcc) phase-lines of the critical nuclei, with cp representing either of the closed-packed phases fcc or hcp. It requires the knowledge of the Turnbull coefficients, latent heats and melting temperatures of all phases of interest, in our case bcc, fcc, and hcp. All these quantities have been explicitly determined previously in this paper except α_{hcp}. It is expected to be very similar to α_{fcc} but larger. We have solved Eq. 12 assuming $\alpha_{\mathrm{hcp}} = \alpha_{\mathrm{hcp}} = 0.54$, and the resulting T_{fcc}^* and T_{hcp}^* are shown as solid lines in Fig. S8. The nucleation phase line $T^*(P)$ is the minimum of T_{fcc}^* and T_{hcp}^* at every pressure, and is shown in Fig. 5 of the main text. The triple point pressure where $T_{\mathrm{fcc}}^* = T_{\mathrm{hcp}}^*$ is at 71.9 GPa, where $T^* = 3263$. Fig. S8 also shows how T_{hcp}^* change if α_{hcp} is significantly increased to 0.56. This is shown by the dashed line in Fig. S8, where the triple point has now moved up to nearly 74 GPa. This constitutes a 2 GPa uncertainty in the location of the fcc-bcc-hcp coexistence point of the critical solid nuclei embedded in the melt.

Kinetic stability of postcritical clusters

We intend to study below the kinetic stabilities of postcritical nuclei by simulating their growth via MD simulations within the NPT ensemble. As described in the main text, this study involves three steps: (i) preparing atomistic configurations of critical solid-phase clusters embedded in the melt at different undercooling temperatures, (ii) initiating dynamic trajectories from these configurations, and (iii) characterizing the evolution of their solid-phase content as the solid clusters grow. The most difficult task is the preparation of critical clusters at large undercoolings. The method implemented here, which is described below, is only one of many approaches. Certainly bias-potential methods using bond-orientational order parameters as employed in the past in e.g. (6) and (9) can be quite effective in this regard.

For the present study we have followed the following protocol:

1. Start with a metastable bcc-liquid equilibrium in the core of the MSCL domain, obtained through the closed-ensemble (NPH) technique.

2. Shrink the cluster slowly within the NPH ensemble by smoothly and reversibly increasing the system's enthalpy H_{sys}.

3. Above a threshold value for the system's enthalpy $H_{\mathrm{sys}} > H_{\mathrm{SL}}^{\mathrm{th}} < H_L^m$, where H_L^m is the liquid enthalpy at the melting point, the solid-liquid coexistence becomes unstable and solid-phase clusters shrink and vanish, eventually leaving a homogeneous liquid behind.

4. Store solid-liquid configurations along the shrinking trajectory. For each configuration, identify the cluster size N_{S} and the coexistence temperature $T_c(N_{\mathrm{S}})$. The latter is determined by switching to the NPT ensemble, and finding the temperature above which the cluster shrinks, and below which the cluster grows.

5. Find the smallest cluster size N_u, which grows to large sizes in the bcc phase without phase transformation. Smaller clusters of size $N_{\mathrm{S}} < N_u$ with coexistence temperatures $T_c(N_{\mathrm{S}}) < T_c(N_u) = T_u$, exhibit phase transformation to fcc/hcp when growing. In this way, we identify for every pressure P, the lower bound $T_u(P)$ to the kinetic stablility of bcc-phase clusters. Below this temperature, the growing bcc nuclei readily transform to close-packed structrues.

We have performed the above procedure for bcc-MSCL in 314928-particle computational cells and have extracted $T_u(P)$ at four pressures: 20, 30, 40, and 60 GPa. We have thus found that at large undercoolings, the growing bcc nuclei become structurally unstable towards phase transformation to the more stable close-packed phases. An illustrative example is shown in Fig. S9, which depicts a solid critical cluster at 30 GPa on the verge of dynamic instability. It was obtained by slowly shrinking a metastable bcc cluster in the NPH ensemble down to 200 particles with predominantly bcc symmetry. When growing this cluster at 1860 K in the NPT ensemble, it transitions to the fcc phase. However, at 1863 K, it grows to large sizes in the bcc phase. The conventional explaination for this instability is that the bulk bcc phase becomes dynamically unstable at sufficiently low temperatures (large undercoolings). As a contrast, we show below that fast interface kinetics can generate far-from-equilibrium nuclei outside the scope of CNT that can have reduced kinetic barriers towards solid-solid phase transformations. This mechanism is explicitly non-equilibrium and interface-driven and cannot be traced to the dynamical structural properties of the bulk crystal phase alone.

An example of such a transformation is shown in Fig. S10. An 800-particle mixed fcc/hcp-phase critical cluster, is obtained by shrinking a mixed fcc/hcp solid-liquid equilibrium, see Fig. 4(d), in the NPH ensemble at pressure $P = 70$ GPa. Growing this cluster by MD simulations in the NPT ensemble at the coexistence temperature $T_c = 2800$ K, causes partial transformation to the bcc phase shown in Fig. S10(a). Slightly larger critical clusters at coexistence temperatures above 2800 K do not exhibit structural transformation to bcc. It is hard to explain the partial transition to bcc, shown in Fig. S10(a), by energetic arguments purely based on the dynamical stability of the bulk bcc crystal. The reason for this is that the bcc phase is entropically stabilized at high temperatures with respect to the fcc phase, and therefore becomes only less stable as temperature is lowered. Hence, a mechanism involving explicit liquid-solid interface structure and dynamics must be invoked. We illustrate the role of interfacial kinetics in driving the structural phase transformation by simulating the growth of the same 800-atom cluster starting at the coexistence temperature $T_c = 2800$ K, but this time the growth rate is slowed down by continuous heating at a rate of 0.5 K/ps. The end result of this process is shown in Fig. S10(b), where it can be observed that the slower growth rate has suppressed transformation to bcc.

Extraneous-phase interface layers: Interfacial phase transformations and growth mode transitions

The mobilities of the (0001) interfaces in the linear mobility regime outside of the Δ_a temperature interval, were calculated using periodic slab geometries containing 160000 particles composed of $40 \times 20 \times 50$ hcp 4-atom orthorhombic unit cells. The mobilities of the $(11\bar{2}0)$ interfaces were calculated using periodic slab geometries containing 332800 particles composed of $52 \times 50 \times 32$ hcp 4-atom orthorhombic unit cells. All the studies involving the Δ_a temperature interval, the phase transformation and the growth mode transition were based on two-phase simulations in periodic slab geometries containing 640000 particles composed of $80 \times 40 \times 50$ 4-atom orthorhombic unit cells.

References

1. G.J. Martyna, D.J. Tobias, and M.L. Klein (1994) Constant Pressure Molecular Dynamics Algorithms. *J. Chem. Phys.* **101**(5):4177.
2. M. Parrinello, A. Rahman (1981) Polymorphic Transitions in Single Crystals: A New Molecular Dynamics Method. *J. Appl. Phys.* **52**(12):7182-7190.
3. M.E. Tuckerman, J. Alejandre, R. Lopez-Rendon, A.L. Jochim, G.J. Martyna (2006) A Liouville-Operator Derived Measure-Preserving Integrator for Molecular Dynamics Simulations in the Isothermal-Isobaric Ensemble. *J. Phys. A: Math Gen.* **39**(19):5629-5651.
4. W. Shinoda, M. Shiga, M. Mikami (2004) Rapid Estimation of Elastic Constants by Molecular Dynamics Simulation under Constant Stress. *Phys. Rev. B* **69**(13):134103.
5. L.A. Zepeda-Ruiz, B. Sadigh, A. A. Chernov, T. Haxhimali, A. Samanta, T. Oppelstrup, S. Hamel, L.X. Benedict, J.L. Belof (2017) Extraction of Effective Solid-Liquid Interfacial Free Energies for Full 3D Solid Crystallites from Equilibrium MD Simulations. *J. Chem. Phys.* **147**(19):194704.
6. P.R. ten Wolde, M.J. Ruiz-Montero, D. Frenkel (1995) Numerical Evidence for bcc Ordering at the Surface of a Critical fcc Nucleus. *Phys. Rev. Lett.* **75**(14):2714.
7. P.R. ten Wolde, M.J. Ruiz-Montero, D. Frenkel (1996) Numerical Calculation of the Rate of Crystal Nucleation in a Lennard-Jones System at Moderate Undercooling. *J. Chem. Phys.* **104**(24):9932-9947.
8. C. Desgranges and J. Delhommelle (2007) Controlling Polymorphism during the Crystallization of an Atomic Fluid. *Phys. Rev. Lett.* **98**(23):235502.
9. A. Samanta, J. Belof (2018) The Thermodynamics of a Liquid-Solid Interface at Extreme Conditions: A Model Close-Packed System up to 100 GPa. *J. Chem. Phys.* **149**(12):124703.
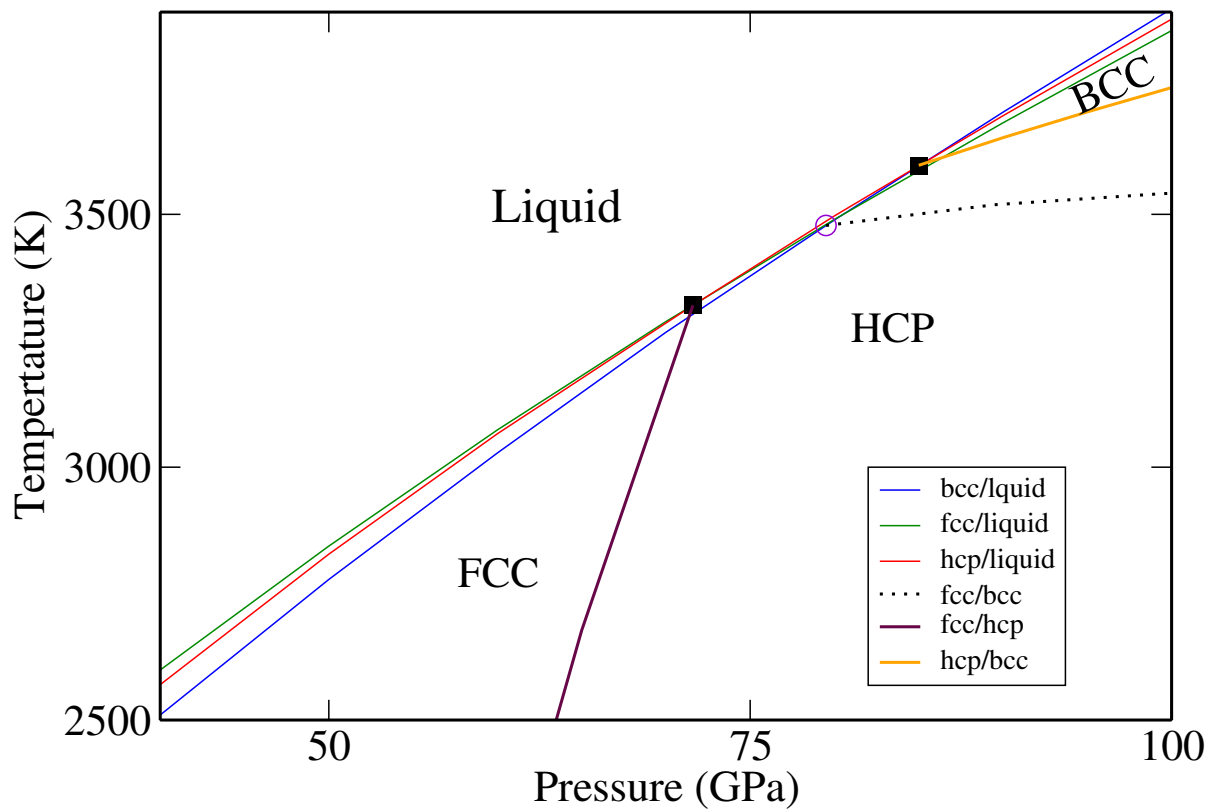
Fig. S1. Detailed temperature-pressure phase diagram of Mishin Cu model. There exist three bulk triple points: (i) liquid-hcp-fcc coexistence at 71.6 GPa and 3320 K, (ii) liquid-fcc-bcc coexistence at 79.5 GPa and 3478 K, and (iii) liquid-hcp-bcc coexistence at 85 GPa and 3598 K. The two thermodynamioc triple points at 71.6 GPa and 85 GPa are marked in the figure by two filled squares. The third triple point at 79.5 GPa is only metastable and is actually in the region of thermodynamic stability of the hcp phase. It is marked in the figure by the open circle.

Babak Sadigh, Luis Zepeda-Ruiz, Jonathan L. Belof
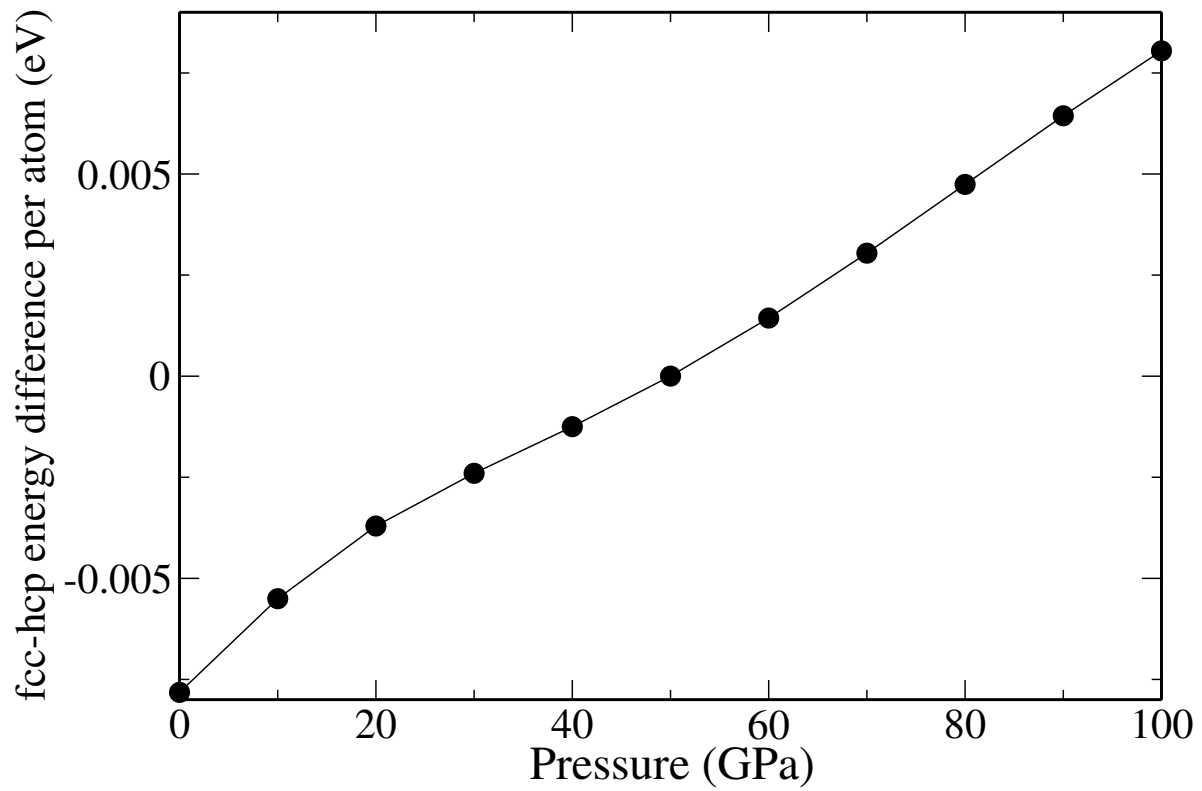
Fig. S2. Energy difference between the fcc and the hcp phases as a function of pressure at 0 K. Note the transition pressure at 50 GPa. Below this pressure fcc is the stable phase, and above it, hcp becomes stable.
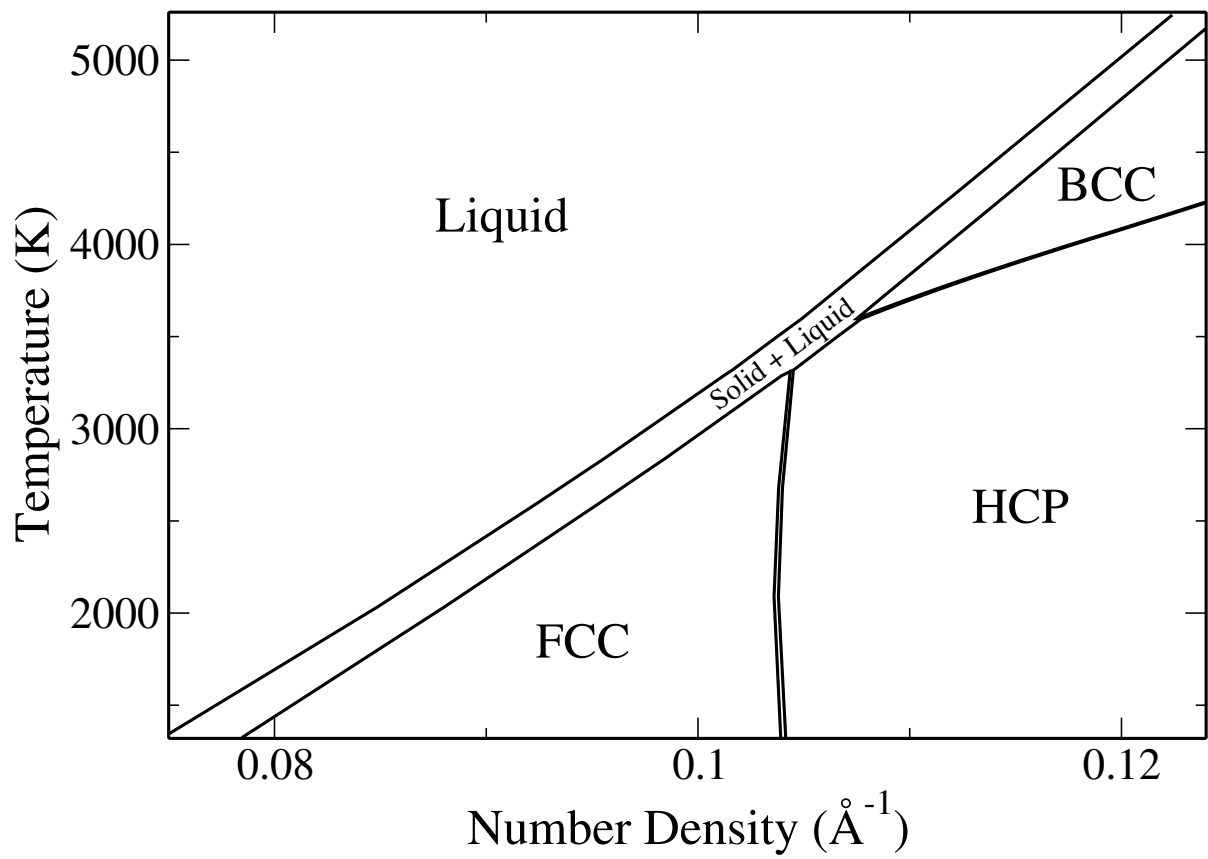
Fig. S3. Thermodynamic phase diagram of the EAM-Cu model in the temperature-density plane. Its representation in the temperature-pressure plane is depicted in Fig. 1 of the main text.

Babak Sadigh, Luis Zepeda-Ruiz, Jonathan L. Belof
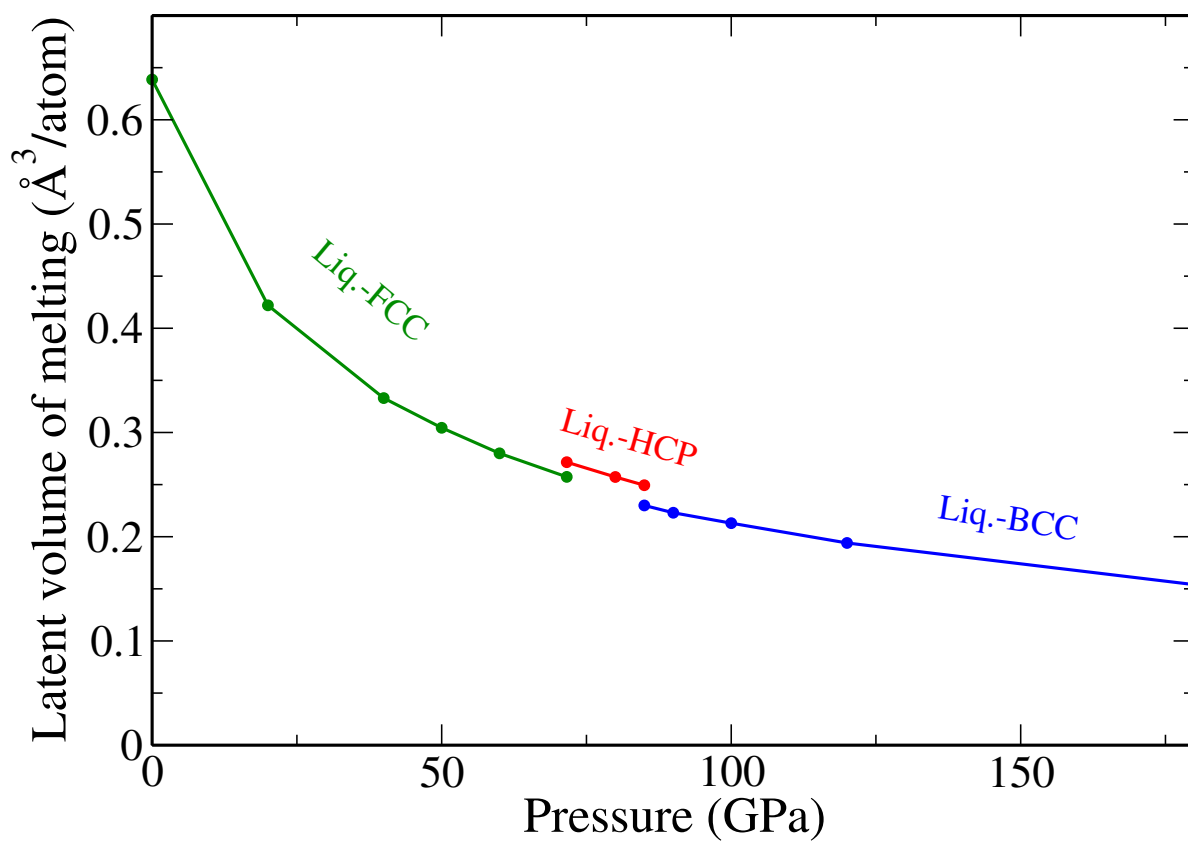
Fig. S4. Latent volumes of melting (the difference in volume between the liquid and the solid phases at coexistence) as a function of pressure. The different colors depict the different solid phases (fcc:green, hcp: red, bcc: blue), from which equilibrium melting occurs.
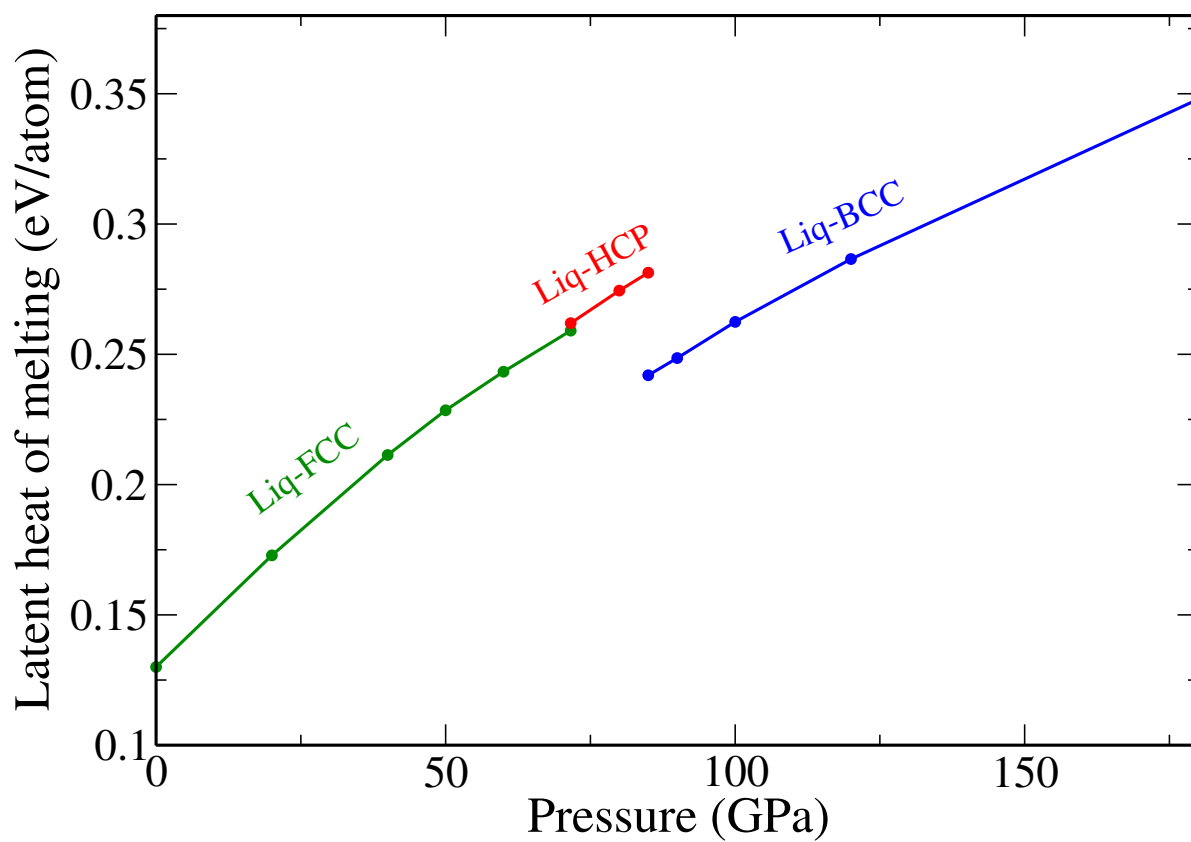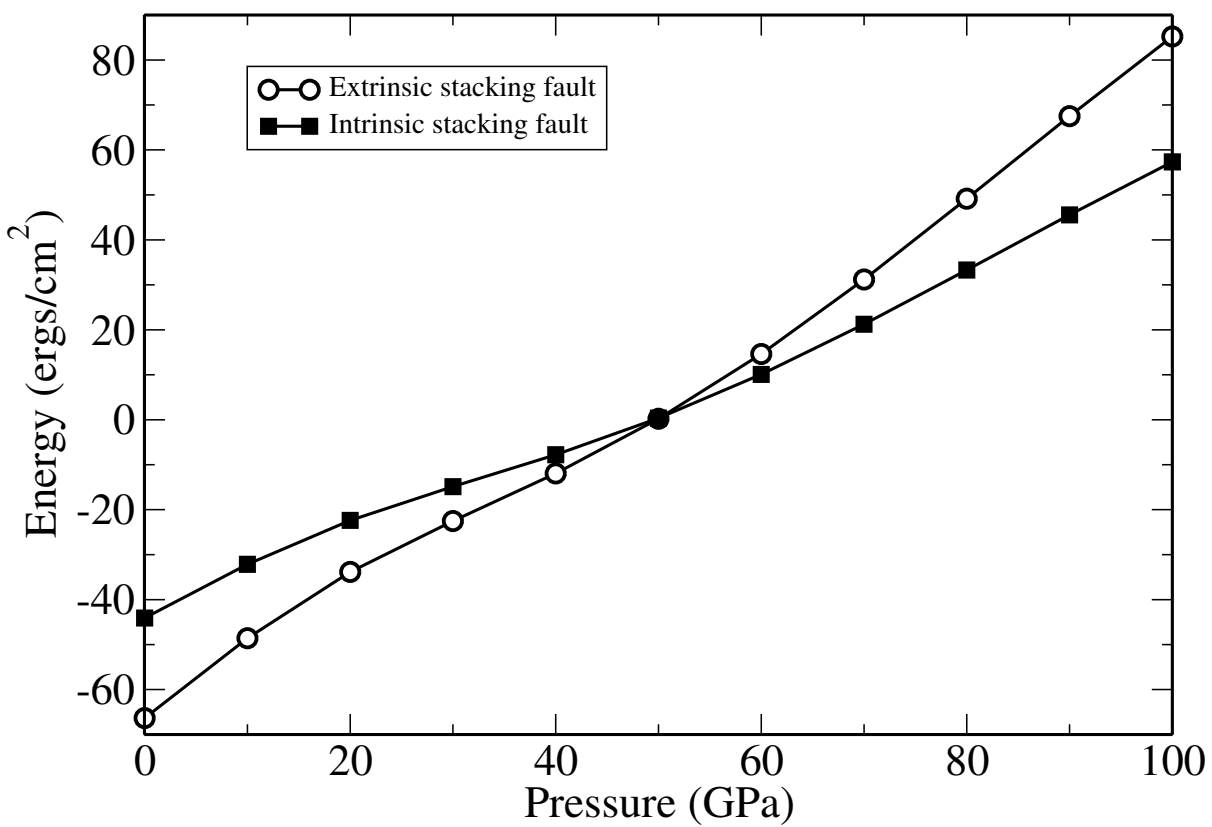
Fig. S5. Latent heats of melting (the difference in enthalpy between the liquid and the solid phases at coexistence) as a function of pressure. The different colors depict the different solid phases (fcc:green, hcp: red, bcc: blue), from which equilibrium melting occurs.

Babak Sadigh, Luis Zepeda-Ruiz, Jonathan L. Belof

Fig. S6. The energies of an extrinsic and an intrinsic stacking fault in the hcp phase at 0 K. The negative energies at small pressures reflect the stability of the fcc phase.
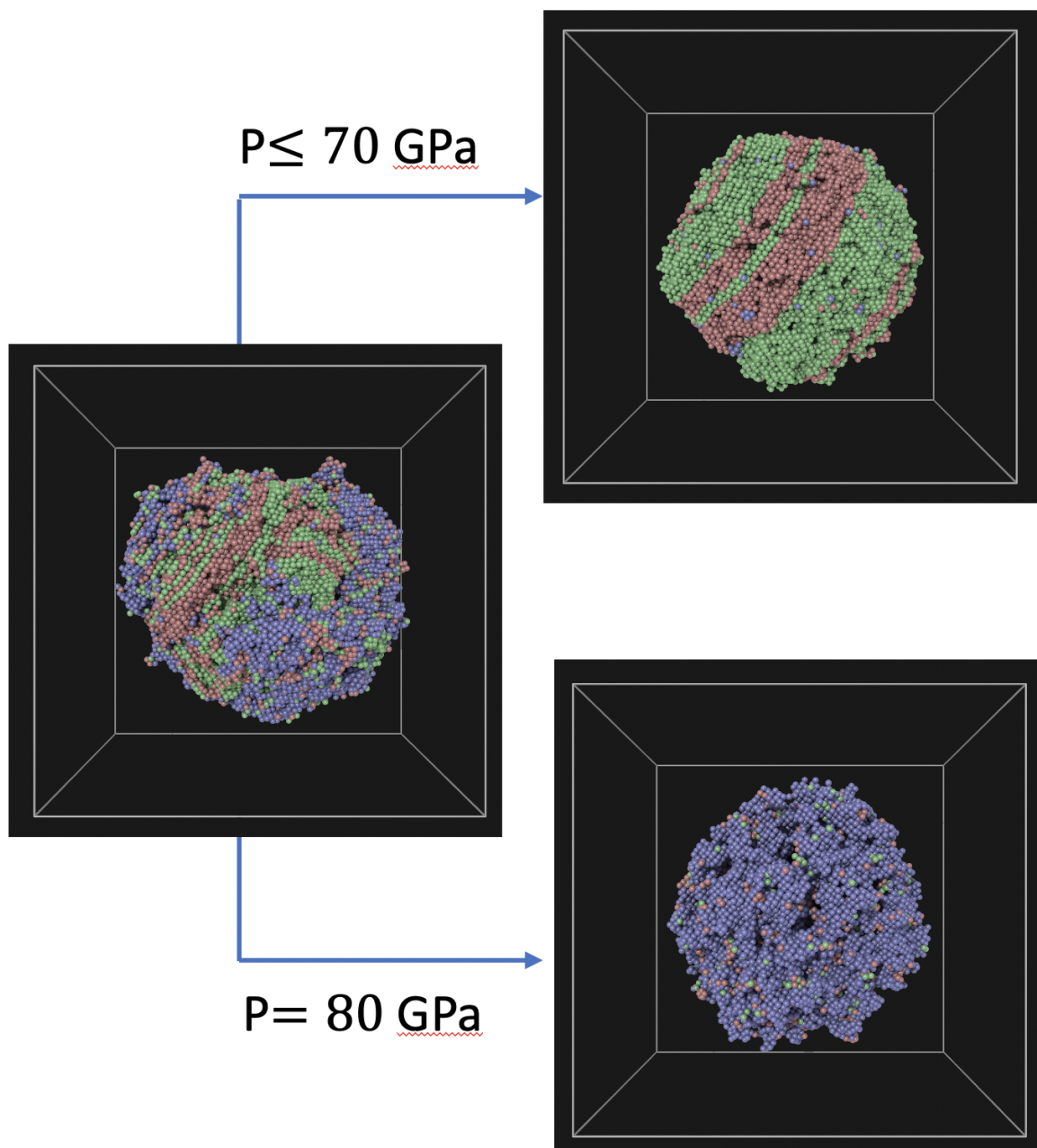
Fig. S7. A mixed bcc-fcc-hcp cluster embedded in liquid obtained from an unstable postcritical bcc cluster at 60 GPa and 2200 K. Upon equilibration in the NPH ensemble, it relaxes into the mixed fcc/hcp metastable-cluster configuration at pressures 70 GPa and below. At 80 GPa it can equilibrate to a bcc cluster configuration in coexistence with the melt.

Babak Sadigh, Luis Zepeda-Ruiz, Jonathan L. Belof
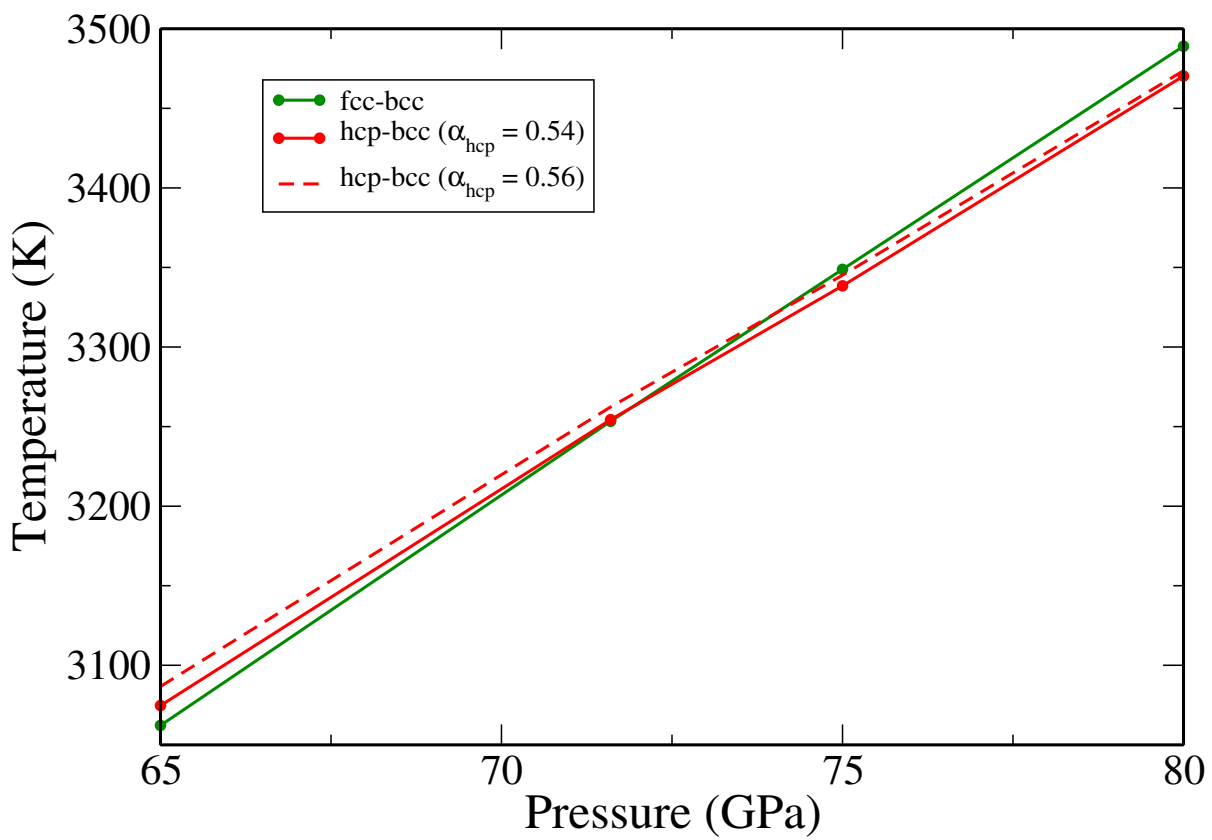
Fig. S8. Solid-nucleation phase boundaries. The solid lines depict $T^*_{\text{fcc}}(P)$ (green) and $T^*_{\text{hcp}}(P)$ (red), assuming $\alpha_{\text{fcc}} = \alpha_{\text{hcp}} = 0.54$. The dashed line shows $T^*_{\text{hcp}}(P)$ for $\alpha_{\text{hcp}} = 0.56$.
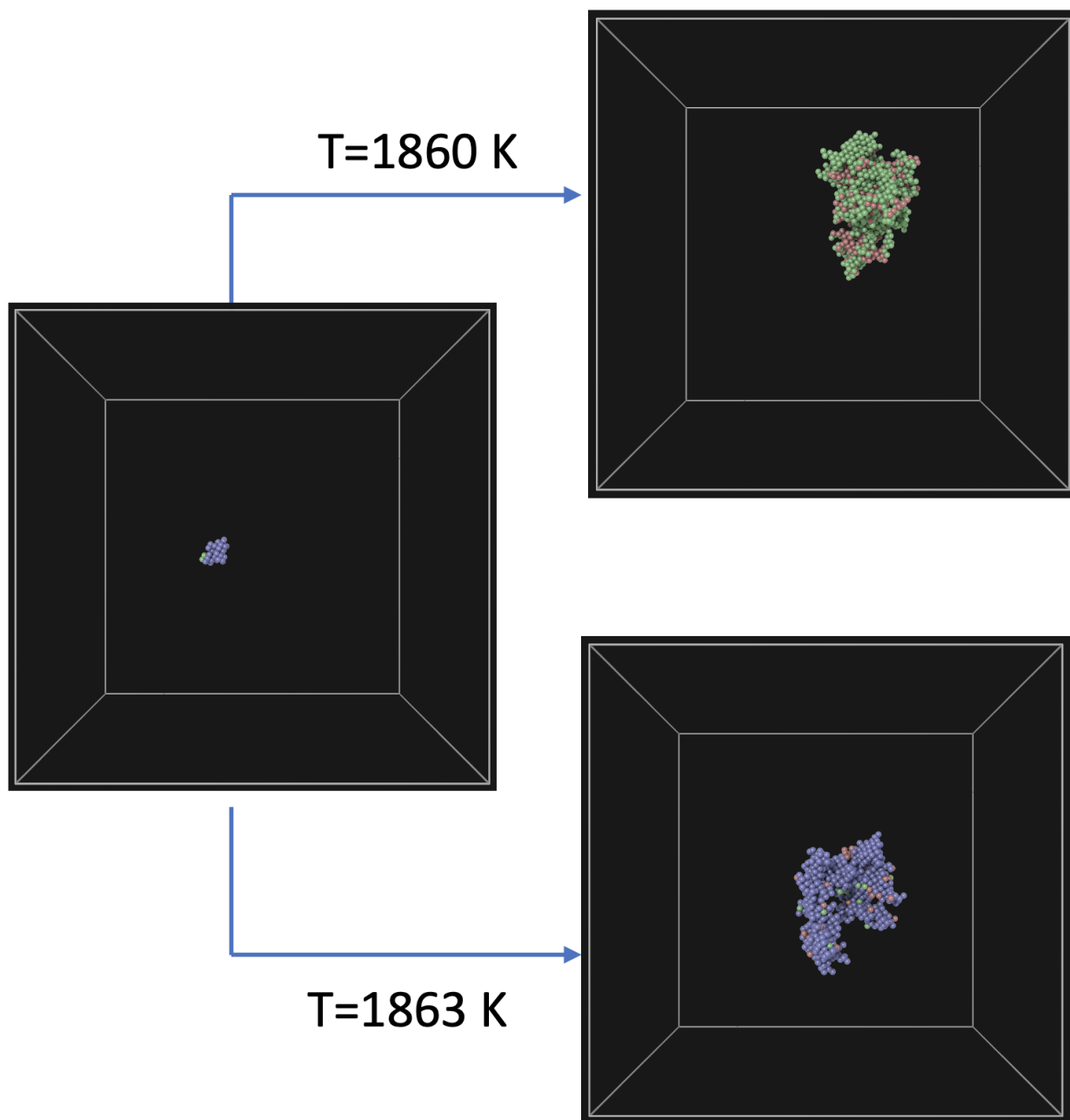
Fig. S9. Example of a bcc critical cluster on the verge of kinetic phase stability. A 200-particle cluster is obtained by continuous shrinking of a metastable bcc cluster, see Fig. 3(b) in the main text, at 30 GPa, via reduction of the total enthalpy of the system in an NPH ensemble. The results of two NPT simulations at 1860 K and at 1863 K is shown. At 1860, the growing cluster transforms to fcc, while at 1863 K, no phase transformation is observed. Particles with bcc symmetry are shown in blue, fcc symmetry in green, and hcp symmetry in red.

**Babak Sadigh, Luis Zepeda-Ruiz, Jonathan L. Belof**
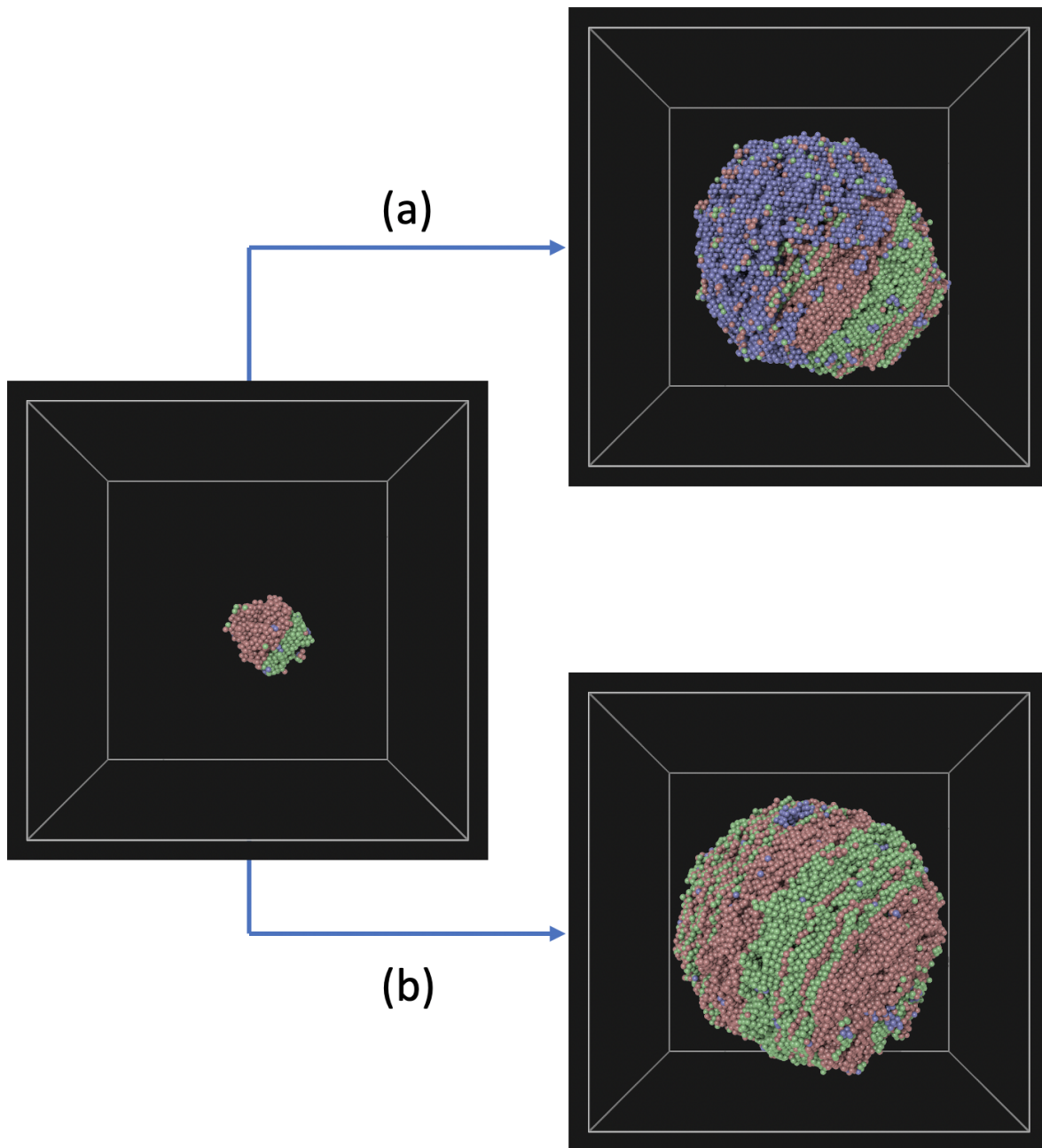
Fig. S10. Example of a far-from-equilibrium solid-cluster-phase evolution. An 800-particle cluster is obtained by continuous shrinking of a mixed fcc/hcp cluster, see Fig. 3(d) in the main text, at 70 GPa, via reduction of the total enthalpy of the system in an NPH ensemble. This cluster shrinks and disappears in NPT ensembles at temperatures above 2800 K. Two simulations of cluster growth are shown: (a) Fast growth NPT simulation at 2800 K, and (b) Slow growth NPT simulation starting at 2800 K, and continuously heated at a rate of 0.5 K/ps. Subsequent annealing of the outcomes of both simulations in an NPH ensemble produces the equilibrium embedded fcc/hcp mixed-phase cluster, shown in Fig. 3(d) in the main text. Particles with bcc symmetry are shown in blue, fcc symmetry in green, and hcp symmetry in red.
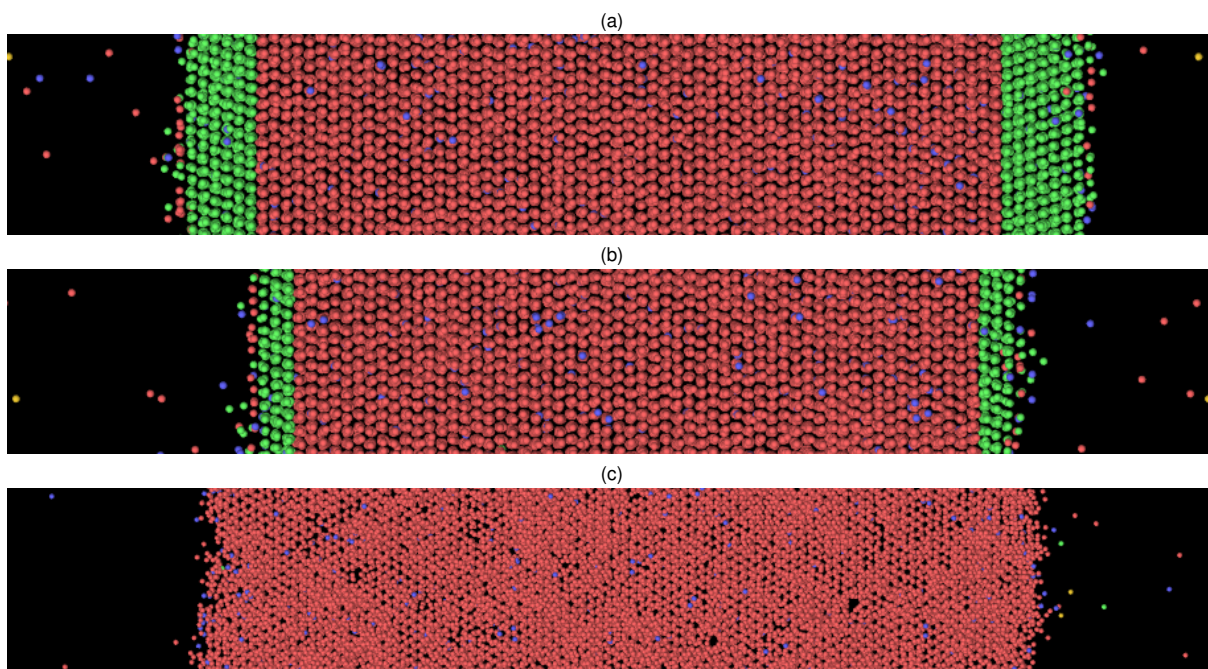
Fig. S11. Side views of liquid-solid slab equilibria at 80 GPa. The bulk crystal phase (red particles) is hcp and the green particles represent occurrence of fcc symmetry mainly at the interface with the liquid. The particle symmetries are classified via adaptive cutoff common-neighbor analysis, and the non-crystalline particles have been deleted. (a) and (b) depict hcp-(0001) interfaces with the liquid. At the liquid interface, the solid transforms to fcc domains with fcc-(111) planes parallel to the interface. The two-phase equilibrium temperatures are (a) 3492 K, and (b) 3500 K. (c) depicts hcp-$(11\bar{2}0)$ interfaces with the liquid at a temperature of 3497 K.

**Babak Sadigh, Luis Zepeda-Ruiz, Jonathan L. Belof**
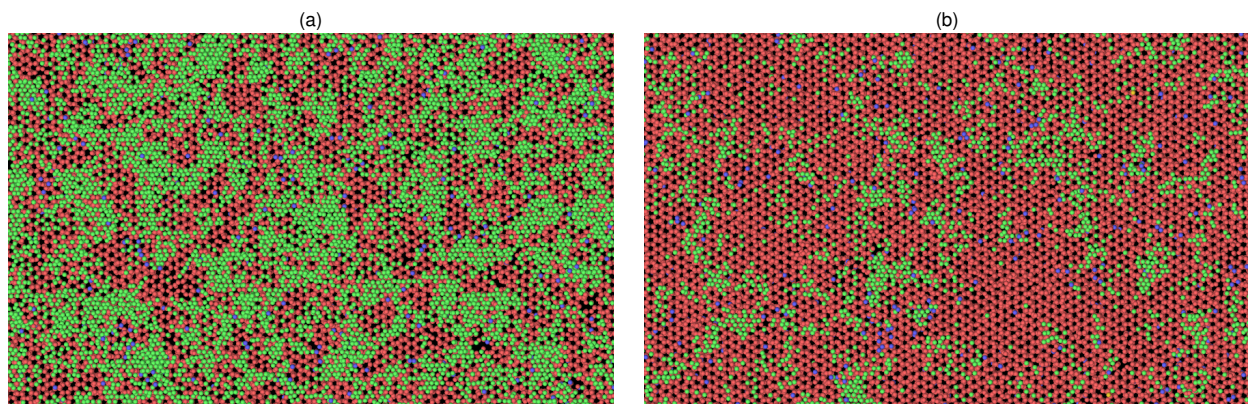
Fig. S12. Top view cross sections of the solid liquid-solid equilibria shown in Fig. S11(a) and (b). The bulk crystal phase (red particles) is hcp and the green particles represent occurrence of fcc symmetry right at the interface. The particle symmetries are classified via adaptive cutoff common-neighbor analysis, and the non-crystalline particles have been deleted.
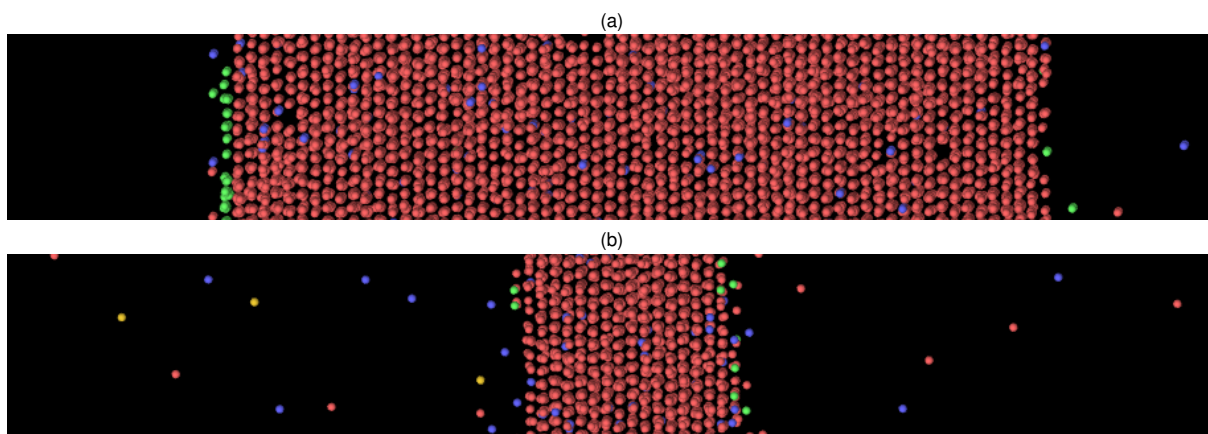
Fig. S13. Side view of two snap shots of a solid-liquid system at 80 GPa with the solid phase shrinking due to superheating at 3520 K. (a) initial configuration, and (b) configuration at about 1 ns later. The particles are classified via adaptive cutoff common-neighbor analysis, with the hcp particles colored red, fcc particles green, and bcc particles blue, The non-crystalline particles have been deleted.

Babak Sadigh, Luis Zepeda-Ruiz, Jonathan L. Belof

(a)

(b)
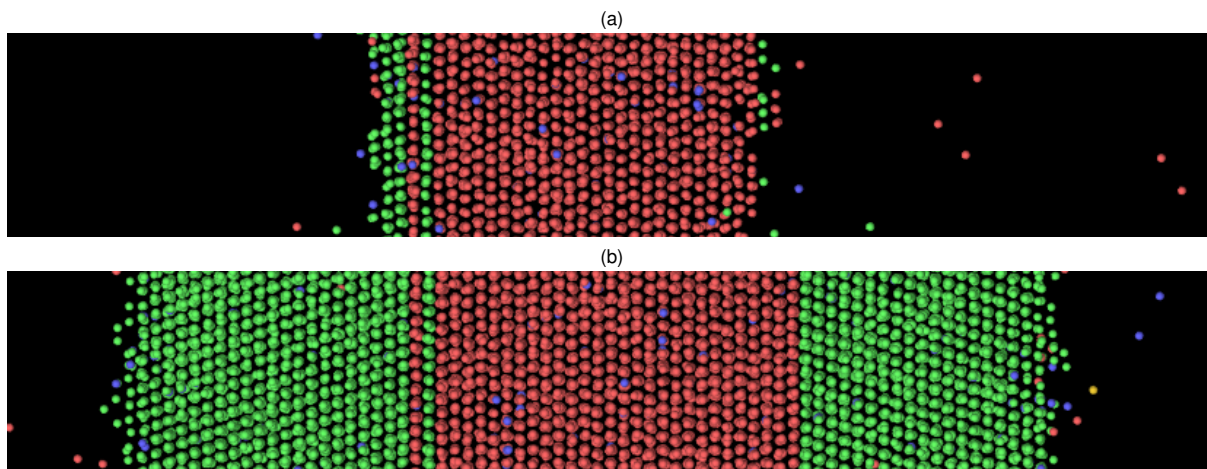
Fig. S14. Side view of two snap shots of a solid-liquid system at 80 GPa with the solid phase growing due to undercooling at 3480 K. (a) initial configuration, and (b) configuration at about 3 ns later. The particles are classified via adaptive cutoff common-neighbor analysis, with the hcp particles colored red, fcc particles green, and bcc particles blue, The non-crystalline particles have been deleted. The close-packed stacking sequence is ..BACBACABAB.. at the left interface and ..ABABCABCAB... at the right one, resulting in the twin relation between the left and the right fcc films.

(a) (b)
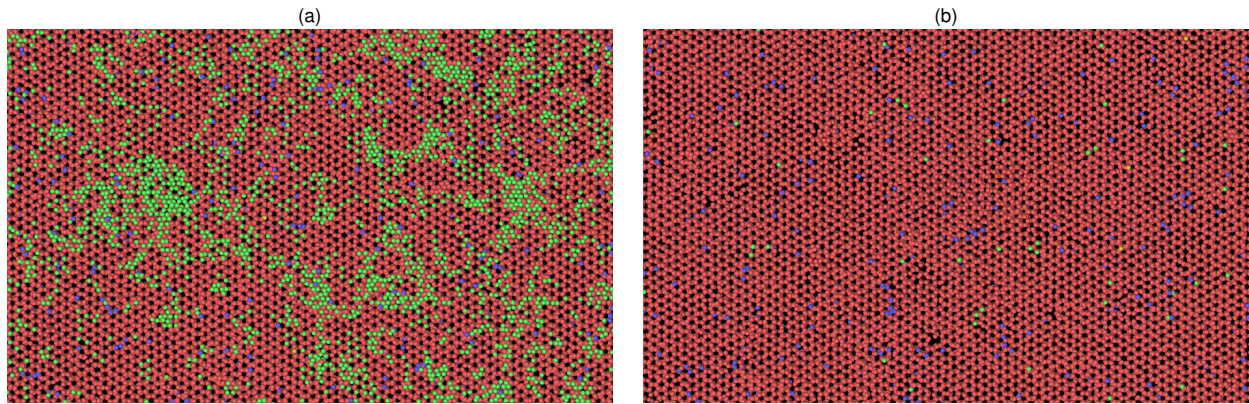
Fig. S15. Top view of cross sections of two snap shots of the NPT-MD simulation at $P = 80$ GPa, and $T = 3503$ K, shown in Fig 8(b) of the main text. The bulk crystal phase (red particles) is hcp and the solid-liquid interface plane is hcp-(0001). The interface contains fcc domains (green particles) with fcc-(111) planes parallel to the interface. The particles are classified via adaptive cutoff common-neighbor analysis, and the non-crystalline particles have been deleted. The two snap shots are (a) initial configuration at time ($t = 0$) in phase II, and (b) the configuration at time ($t = 9.5$ ns) in phase I.

Babak Sadigh, Luis Zepeda-Ruiz, Jonathan L. Belof